Reynolds number scaling of pocket events in the viscous sublayer

M. Metzger,* A. Fershtut, and C. Kunkel
Department of Mechanical Engineering, University of Utah, Salt Lake City, Utah 84112, USA

J. Klewicki
Mechanical Engineering Department, University of New Hampshire, Durham, New Hampshire 03824, USA and Department of Mechanical Engineering, University of Melbourne, Parkville, Victoria 3010, Australia
(Received 6 August 2017; published 15 December 2017)

Recent findings [X. Wu *et al.*, Proc. Natl. Acad. Sci. USA **114**, E5292 (2017)] reinforce earlier assertions [e.g., R. Falco, Philos. Trans. R. Soc. London A **336**, 103 (1991)] that the sublayer pocket motions play a distinctly important role in near-wall dynamics. In the present study, smoke visualization and axial velocity measurements are combined in order to establish the scaling behavior of pocket events in the viscous sublayer of the turbulent boundary layer. In doing so, an identical analysis methodology is employed over an extensive range of friction Reynolds numbers $388 \leqslant \delta^+ \leqslant 2.2 \times 10^5$. Both the pocket width W and time interval between pocket events T increase logarithmically with Reynolds number when normalized by viscous units. Normalization of W and T by the Taylor microscales evaluated at a wall-normal location of about 100 viscous units, however, appears to successfully remove this Reynolds-number dependence. The present results are discussed in the context of motion formation owing to the three dimensionalization of the near-wall vorticity field and, concomitantly, the recurring perturbation of the viscous sublayer.

DOI: 10.1103/PhysRevFluids.2.124602

I. INTRODUCTION

Understanding the physical mechanisms that sustain turbulence production and drag force generation has been of interest in turbulent boundary layer research at least since Theodorsen's introduction of the hairpin vortex model [1] over 65 years ago. Coherent vortical motions, including but not limited to quasistreamwise vortices, hairpin vortices, and so-called typical eddies, are individually and collectively purported to play significant, but varying, roles in both turbulence production and momentum transport [2–9]. Sublayer streaks have been believed to play an integral role in the near-wall self-sustaining bursting cycle that involves the generation and evolution of quasistreamwise vortices [10–12]. Alternatively, Falco [7,13] portrays streaks as the far-field signature of intermediate-scale wallward advecting vortical motions whose stronger near-field interaction culminates with the rapid formation of sublayer pockets. Consistent with this, recent analyses of direct numerical simulations by Wu *et al.* [14] provide convincing evidence that viscous sublayer streaks are passive structures in the near-wall regeneration process and largely symptomatic of the presence of turbulent-turbulent spots in the inner layer. Deciphering the nature of the connection between inner-layer structures and their impact on the sublayer, and hence the skin friction, is of paramount importance for advancing turbulence theory and improving the accuracy of numerical models, especially as the Reynolds number becomes large.

Two main turbulence structures have been observed in the sublayer: streaks and pockets; see Ref. [6] for an overview. Figure 1 illustrates these structures as would be seen by sublayer smoke visualization. A significant feature of the streak motions is that when normalized by viscous scales, their average spanwise streak spacing ℓ_s is apparently invariant with Reynolds number

*Corresponding author: m.metzger@utah.edu

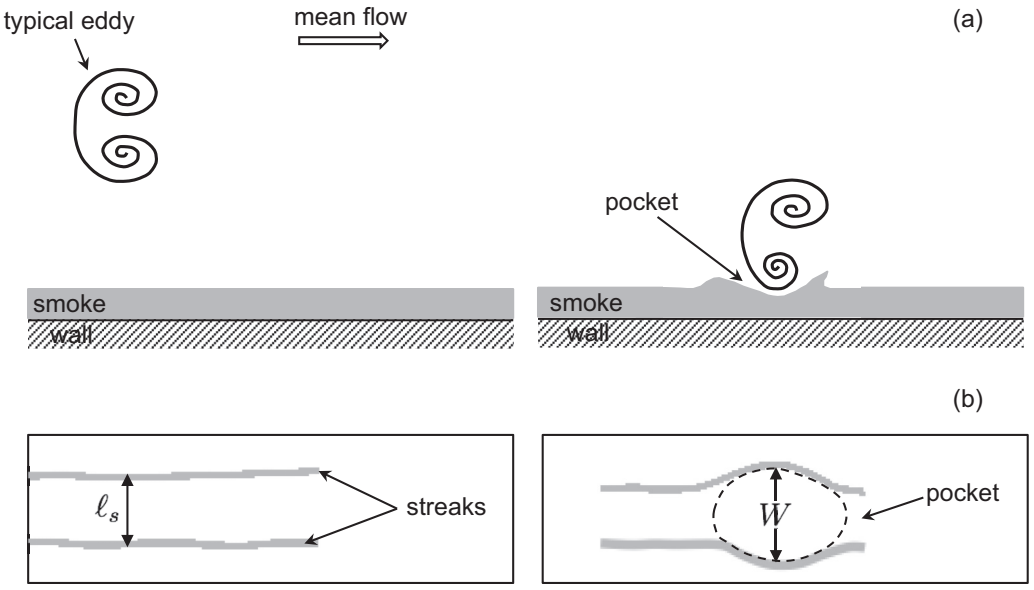

FIG. 1. Idealization of streaks and pocket structures as made visible by smoke visualization of the viscous sublayer: (a) side view, streamwise wall-normal plane, (b) plan view, streamwise-spanwise plane. Note that pockets are quasisymmetrical regions devoid of the tracer, often (but not always) occurring between two streaks. (Adapted from Ref. [7].)

$\ell_s^+ \simeq 100$ [15,16]. Note that a plus sign superscript indicates normalization by the kinematic viscosity ν and the friction velocity u_τ $(=\sqrt{\tau_{\text{wall}}/\rho})$, where τ_{wall} is the mean wall shear stress and ρ is the fluid density. Conversely, while also known to be present in both high- and low-Reynolds number, flows, the inner-normalized size of the pocket motions show variations with Reynolds number $\delta^+ = \delta u_\tau/\nu$, where δ is the boundary layer thickness [15]. If streaks are essentially passive entities in the sublayer as the results by Wu *et al.* [14] suggest, then that would imply that pockets are the predominant dynamically active motions in the viscous sublayer. Such considerations motivate the present study of pocket scaling behaviors.

A considerable and growing body of evidence indicates that, even very close to the wall, a number of inner-normalized turbulence statistics exhibit Reynolds-number dependences [17–19]. The physical origin of some of the observed phenomena has been shown to connect to inner-outer interactions [20], while other studies suggest that these δ^+ dependences are associated with the scaling structure of the mean dynamical equation [21,22] and accordingly the mechanisms of inertial turbulent transport [23]. A relevant observation is that many of these Reynolds-number dependences are approximately logarithmic [17,24,25].

As first observed in flow visualizations [26], when a tracer is continuously injected into the sublayer (via a tangential slot in the wall), pockets are identified in plan view as initially circular and then crescent-shaped regions devoid of tracer. The laboratory measurements of Falco, along with analysis of visualizations conducted on the salt playa of western Utah, indicate that the inner normalized pocket width W^+ and time interval between pockets T^+ increase approximately logarithmically with Reynolds number [7,15]. Although both streaks and pockets are observed in the viscous sublayer, it is reasonable to conclude that, because of the difference in scaling properties between the two types of coherent structures, the mechanisms responsible for low-speed streaks are not identical to those of pockets. Collectively, these considerations motivate the present focus on correlating pocket motion attributes with wall-layer turbulence structure.

Three different physical mechanisms capable of producing pocket formations have been described in the literature [7,27,28]. Falco *et al.* [29] primarily considered pockets as footprints of so-called

typical eddies (identified from flow visualizations as spatially compact regions of concentrated vorticity having a ringlike configuration [30]) that propagate in the outer region and in some cases advect toward the wall. Smith *et al.* [27] observed pocket-type events during the formation and lift-up of hairpin vortices, in between the vortex legs and behind the vortex head. In their direct numerical simulation (DNS) interrogation, Robinson *et al.* [28] found that local regions of high pressure coincide with the spanwise divergence of streamlines in the sublayer, indicative of wallward moving fluid and pocket formations. This connection between pressure fluctuations and pocket events is corroborated by the high-Reynolds-number pressure measurements of Klewicki *et al.* [25]. In that study, the peak in the spectra of the fluctuating wall pressure gradient (both streamwise and spanwise gradients) was found to be consistent with the characteristic length scale of pockets at similar Reynolds number. Note that wall pressure gradients are important because they provide a mechanism for the surface flux of vorticity [31] and thus likely play a critical role in the near-wall self-sustaining process of the turbulence.

Potentially significant common attributes of the pocket forming physical mechanisms described above are the presence of positive absolute spanwise vorticity ω_z, i.e., having a sign opposite to that of the mean vorticity $-\partial U/\partial y$, in conjunction with a high-pressure perturbation giving rise to a localized region of high-pressure gradients along the wall. Two-point correlations of spanwise vorticity for probe separations in the wall-normal direction at low Reynolds number reveal the regular occurrence of opposing sign ω_z motions in the near-wall region [32]. Similar, albeit more limited, measurements provide evidence that this structural feature is preserved at $\delta^+ = O(10^5)$ [24]. These behaviors are compatible with the expected vorticity distribution of a typical eddy [7] as well as the generation of positive ω_z under a shear layer motion as it rolls up to form a hairpinlike vortex [27,33]. Consistent with the increasing probability of positive ω_z motions with wall-normal distance [34,35], analysis of DNS data indicates that there is a rapid transfer of mean enstrophy to fluctuating enstrophy in the region $5 \lesssim y^+ \lesssim 50$ that coincides with the rapid three dimensionalization of the overall vorticity field [36]. Accordingly, into the logarithmic region and beyond, the motions bearing positive ω_z increasingly gain parity with those bearing negative ω_z [36,37].

In his physical model, Falco [7] proposes that the positive ω_z motions characteristic of the outer region advect toward the surface at (generally) shallow angles and through the subsequent interaction with the surface produce the pocket motions. In support of this picture, plan-view flow visualizations simultaneous with hot-wire measurements in the buffer layer reveal large negative contributions to the Reynolds shear stress (associated with the wallward movement of high-momentum fluid) coincident with pocket formations [26]. Outside of the sublayer ($y^+ > 10$), measurements at both high and low δ^+ indicate that the duration of spanwise vorticity events with large positive fluctuation (magnitude greater than 1 rms) scale according to the local Taylor time scale [32,36]. Note that this threshold level guarantees that nearly all of the positive detected events have positive ω_z. The present paper provides evidence that the average pocket width W and time interval between pockets T also scale with the Taylor microscales evaluated in the near-wall region, but just beyond where the mean-to-fluctuating enstrophy transfer mentioned above occurs. An important feature of the present study is that the friction Reynolds number varies over three orders of magnitude, achievable through a combination of laboratory and field experiments.

II. EXPERIMENTAL METHODS

The present flow visualization experiments were conducted in the boundary layer wind tunnel located in the Fluid Mechanics Laboratory at the University of Utah. Three different Reynolds numbers were investigated: $\delta^+ = 1131$, 1977, and 3050. Theatrical fog was injected through a thin, nearly tangential slot in the wind tunnel floor and illuminated with a horizontal laser sheet using an argon-ion laser (5 W, Spectra-Physics 2000). The height of the laser sheet was positioned 2 mm above the floor of the wind tunnel, which corresponds to a wall-normal distance of 10–34 viscous units across the three Reynolds numbers investigated. Plan-view flow visualization images were captured at 500 frames/s with a motion picture camera (Red Lake 16 mm) positioned above the transparent

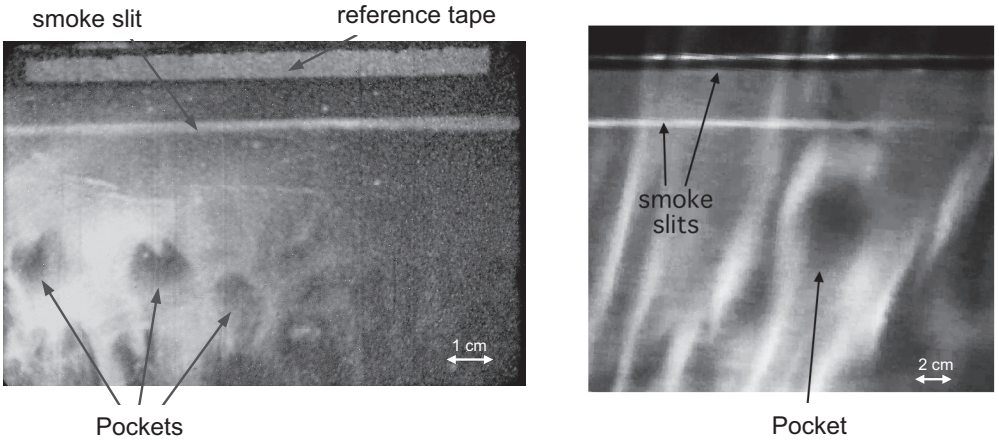

FIG. 2. Sample snapshots of sublayer smoke visualization with several pocket events identified: wind tunnel (left) and atmospheric surface layer (right). The corresponding physical scale is indicated in each case. Flow is from top to bottom.

wind tunnel ceiling. A sample frame from the video is shown in Fig. 2. The friction velocity at each δ^+ was determined using the Clauser method, based on mean velocity profile measurements from a hot wire. Further details regarding the laboratory experiments are given by Fershtut [38].

The field experiments were performed in the atmospheric boundary layer that flows over the salt flats of Utah's western desert. Flow visualizations of the sublayer were accomplished using floodlighting, a CCD camera (60 frames/s), and a buried reservoir that allowed theatrical fog to seep through a tangential slot made flush with the desert floor. Note that the camera lens was focused on the top surface of the slot. Plan-view images of the sublayer were captured during sunset as the atmosphere transitions through neutral thermal stability (during which buoyancy effects become negligible). The local friction velocity was estimated using a hot-wire rake capable of measuring the velocity gradient near the surface. Further details of the field study are described by Klewicki *et al.* [15]. The Reynolds number associated with the atmospheric boundary layer was estimated as $\delta^+ \approx 2.2 \times 10^5 \pm 11\%$ using the local friction velocity and kinematic viscosity along with an estimate of the surface layer depth based on the work of Metzger *et al.* [39].

The average pocket width and time interval between pocket events were measured using identical analysis techniques for the laboratory and field data, namely, those described in [15]. Important features of this methodology are summarized here. To obtain pocket width data, a horizontal reference line was drawn on the video monitor at arbitrary distances of 3 cm (wind tunnel) and 6 cm (atmosphere). For all pockets passing through the reference line, a precision rule was used to measure the maximum width between the centers of concentrated fog lines outlining the crescent-shaped pocket pattern. From the field data, 869 pockets were measured, while from the laboratory data, 200 pockets were measured at each δ^+. The average time interval between pocket events was determined by dividing the total number of pockets detected by the total time elapsed during the interrogation period. The inner normalized time interval was then weighted by the ratio $2\,W^+/Z^+$, where Z^+ represents the inner normalized screen width. This weighting allows T^+ to be interpreted as the inner normalized time interval between events that would be detected by an imaginary probe located at a fixed y^+ in the measurement plane. Note that the exact wall-normal location of the measurement plane for the present flow visualization data remains somewhat ambiguous, but is believed to be in the region $10 \leqslant y^+ \leqslant 30$ based on agreement with the prior work of Falco [7,26]. Although a slightly different method was used to determine T^+ in the study of Klewicki *et al.* [15], renewed analysis of their data using the present method [38] yields results essentially identical to those originally published in [15].

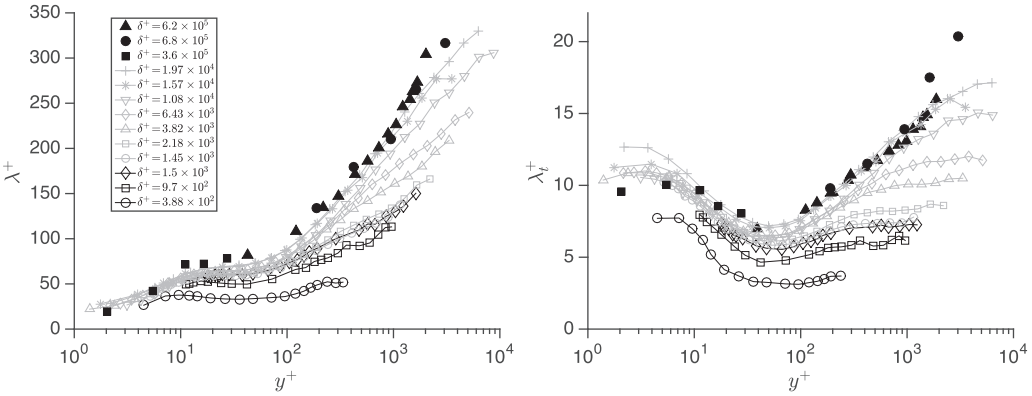

FIG. 3. Inner normalized profiles of the Taylor microscales: Taylor length scale (left) and Taylor time scale (right). Closed symbols ■, ●, and ▲ represent the field data from Metzger [40] acquired over three different years; gray open symbols are laboratory data from Vincenti *et al.* [41] and black open symbols are laboratory data from Klewicki [42].

In the present study, Taylor microscales are used to normalize W and T. Here λ and λ_t denote the Taylor length and time scale, respectively. For reference, profiles of λ^+ and λ_t^+ as a function of δ^+ and y^+ are shown in Fig. 3 over a range of Reynolds numbers spanning three decades. In the case of the Taylor length scale, λ^+ increases nearly monotonically with y^+ at each Reynolds number, except for a short plateau region between $10 < y^+ < 100$. On the other hand, in the case of the Taylor time scale, the λ_t^+ versus y^+ profiles exhibit a local minimum near $y^+ \approx 50$. The data also reveal apparent Reynolds-number trends. For any given $y^+ > \sim 5$, both λ^+ and λ_t^+ increase with δ^+. One can observe different regimes where the Reynolds-number behavior changes. For example, both λ^+ and λ_t^+ increase more dramatically with δ^+ in the logarithmic region $y^+ > \sim 200$, whereas δ^+ variations are less pronounced closer to the wall. In the viscous sublayer, λ^+ appears to be independent of Reynolds number. Later, evidence is given that the pocket width W and time interval between pockets T scale with the Taylor microscales using values for λ and λ_t in the region $\sim 50 < y^+ < \sim 100$. Note that this scaling region corresponds approximately to the region in the y^+ profile where λ_t^+ exhibits a local minimum and λ^+ exhibits a plateau.

Specific details regarding the laboratory and field experiments, from which the hot-wire data in Fig. 3 were taken, are provided elsewhere [40–42]. Note that, since the field data were acquired over different years, the friction Reynolds numbers for each data set are not the same. Specifically, the atmospheric flow visualizations are characterized by a Reynolds number of $\delta^+ = 2.2 \times 10^5$, whereas the Taylor microscale measurements from the atmosphere are characterized by slightly larger Reynolds number (for the hot-wire data over three different years, $2.6 \times 10^5 \leqslant \delta^+ \leqslant 4.6 \times 10^5$, $5.7 \times 10^5 \leqslant \delta^+ \leqslant 7.9 \times 10^5$, and $5.9 \times 10^5 \leqslant \delta^+ \leqslant 6.5 \times 10^5$, respectively). The effect of this on scaling pocket width W and the time between pocket events T is discussed in the next section.

For both the laboratory and field studies, the Taylor length is estimated based on the relation $\lambda^2 = \langle u^2 \rangle / \langle (\partial u / \partial x)^2 \rangle$, assuming isotropic turbulence [43], where u is the fluctuating velocity along the streamwise coordinate x. Here $\langle \cdot \rangle$ denotes a long-time temporal average. Furthermore, the instantaneous velocity signal is decomposed into its mean U and fluctuating components u such that $\langle u \rangle = 0$. The derivative is evaluated using Taylor's frozen turbulence hypothesis along with a Savitzky-Golay filter. Note that the data of Klewicki [42] indicate that outside of the buffer layer the assumption of isotropy provides a good estimate of λ. The Taylor time scale, on the other hand, is determined using an osculating parabola fit to the autocorrelation of u at zero time lag. Therefore, calculation of λ_t does not rely on the assumption of isotropy.

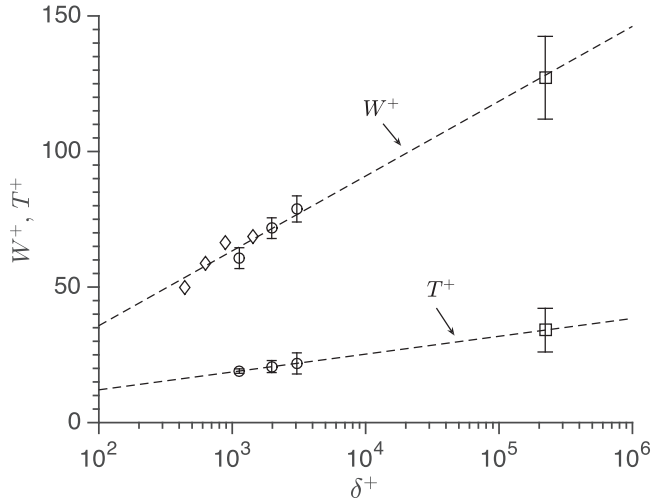

FIG. 4. Reynolds-number dependence of the inner normalized pocket width W^+ and time interval between pockets T^+ from the present work, ○; Ref. [7], ◇; and Ref. [15], □, with logarithmic curve fits.

III. RESULTS

Figure 4 shows the present W^+ and T^+ data as a function of δ^+. For comparison, the W^+ data from Falco [7] over a Reynolds-number range $400 < \delta^+ < 1500$ are also shown. The present low-Reynolds-number W^+ data agree remarkably well with those of Falco. Curve fits to the data reveal a logarithmic Reynolds-number dependence of the inner normalized pocket width and time between pockets that are respectively well approximated by

$$W^+ = 27.6 \log \delta^+ - 19.5, \tag{1}$$

$$T^+ = 6.6 \log \delta^+ - 1.1. \tag{2}$$

The error bars in Fig. 4 represent 95% confidence intervals for each data point, based upon the standard deviation of the mean. The uncertainty in the field data is about twice as large as that of the laboratory data, due to the increased uncertainty in measuring the friction velocity associated with the atmospheric boundary layer. In addition, the width of the square markers used for the atmospheric data corresponds to the uncertainty in δ^+ for those data.

Since inner normalizations show mild (logarithmic) but apparent δ^+ dependences for W and T, three other types of normalizations were investigated. These include (i) outer scaling using normalization based on the boundary layer thickness δ and freestream velocity U_∞, i.e., W/δ and $T\,U_\infty/\delta$, (ii) mesoscaling using normalization based on intermediate length and time scales defined by the geometric mean between the inner and outer scales, i.e., $W^+/\sqrt{\delta^+}$ and $T^+/\sqrt{\delta^+/U_\infty^+}$, and (iii) Taylor scaling using normalization based on the Taylor microscales, i.e., W/λ and T/λ_t. Note that the mesoscaling is, for example, inspired by the scalings associated with the mean momentum balance as shown by Wei *et al.* [21].

The performance of inner scales, outer scales, mesoscales, and Taylor scales in terms of removing δ^+ trends in T and W is presented in Fig. 5. The normalized data (denoted generically by $\tilde{T}$ and $\tilde{W}$) are plotted for convenience on log-log coordinates, which is not necessarily meant to imply power-law behavior. For example, the goodness-of-fit parameter R^2 associated with logarithmic and power-law curve fits to W^+ are 0.9998 and 0.9936, respectively, indicating that a logarithmic function

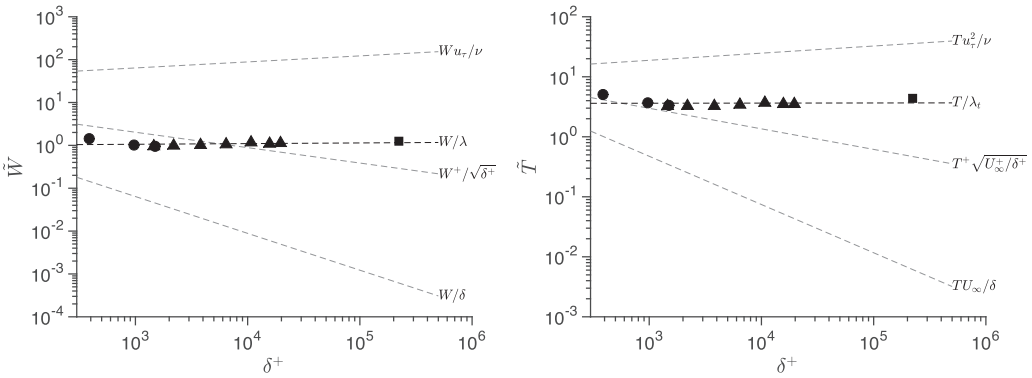

FIG. 5. Scaling the pocket width (left) and time interval between pockets (right). Circles and triangles indicate laboratory data and squares indicate field data. The dashed lines represent power-law curve fits.

of δ^+ fits the W^+ data slightly better than a power law. Clearly under the *proper* normalization, $\tilde{T}$ and $\tilde{W}$ versus δ^+ will appear on the log-log plot as straight lines having zero slope.

In Fig. 5, the gray dashed lines representing the inner scalings, outer scalings, and mesoscalings of $\tilde{W}$ and $\tilde{T}$ follow directly from the empirical expression for W^+ and T^+ in (1) and (2), respectively. For the outer scalings and mesoscalings of $\tilde{T}$, values of U_∞^+ from the hot-wire data were also used. The black markers represent Taylor scaling derived from the hot-wire data shown in Fig. 3. For each δ^+ data set, W^+ and T^+ are determined based on the empirical relations in (1) and (2), respectively; then these values are normalized by the corresponding λ^+ and λ_t^+ obtained from the hot-wire data. In Fig. 5, λ^+ and λ_t^+ are evaluated at a *fixed* location of $y^+ = 100$ for all δ^+. However, one would obtain nearly identical results using values of λ^+ and λ_t^+ at any y^+ in the range $50 \leqslant y^+ \leqslant 200$. This is highlighted below and the physics associated with this observation is discussed further.

The dashed lines in Fig. 5 represent power-law relations of the form

$$\tilde{W} = \alpha\,(\delta^+)^A, \tag{3}$$

$$\tilde{T} = \beta\,(\delta^+)^B. \tag{4}$$

In order for $\tilde{W}$ and $\tilde{T}$ to be independent of δ^+, one seeks a normalization whereby $A \approx 0$ and $B \approx 0$, which would yield a line with zero slope (when plotted in log-log coordinates). As apparent, normalization by the Taylor microscales yields $\tilde{T}$ and $\tilde{W}$ values that are essentially independent of Reynolds number. From this, one can obtain the Reynolds-number-invariant scaling relations

$$\frac{W}{\lambda(y^+{=}100)} = C_1, \tag{5}$$

$$\frac{T}{\lambda_t(y^+{=}100)} = C_2\,, \tag{6}$$

where C_1 and C_2 are constants with values (based on curve fits to the present data) of 0.8 and 3.8, respectively. Interestingly, Metzger *et al.* [44] also found that the local Taylor microscale succeeds in removing both Reynolds number and y^+ trends in the statistical mode of the bursting period (over a similar δ^+ range). The connection between bursts and pockets can be made loosely through the hairpin vortex packet paradigm [9]. Another interesting correlation stems from the recent work of Klewicki *et al.* [25], which showed that the characteristic length associated with surface-pressure gradient perturbations also corresponds to the mean pocket width. Furthermore, Priyadarshana and Klewicki [45] revealed that Reynolds-number effects in the spanwise vorticity spectra at $y^+ = 320$ can be scaled by normalizing the frequency with the local Taylor microscale (the data from their

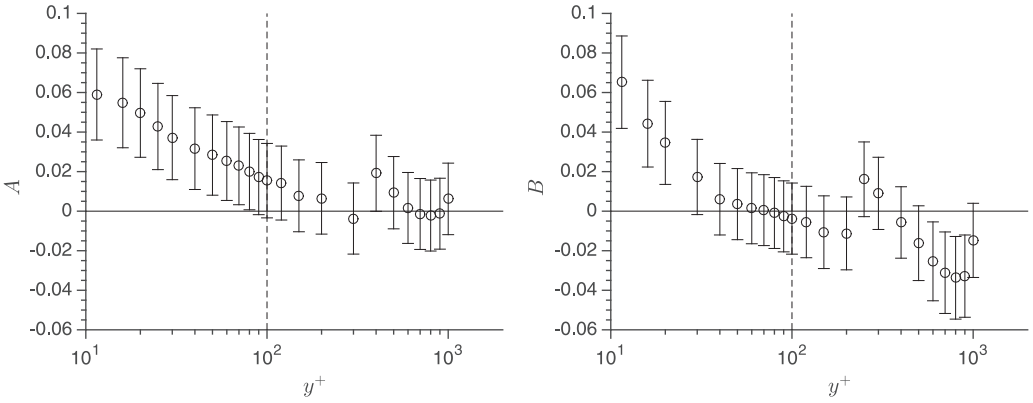

FIG. 6. Slope of the curve fits represented by (7) and (8) as a function of y^+ for W/λ (left) and T/λ_t (right), respectively. The vertical dashed lines delineate $y^+ = 100$, the wall-normal location used in the Taylor normalization of Fig. 5.

study also spanned over three decades in δ^+). Note that, in the context of the present discussion, the difference between $y^+ = 320$ and $y^+ = 100$ is relatively insignificant (see Fig. 6).

Since λ and λ_t are functions of y^+, there is some question as to which y^+ location should be used to evaluate the Taylor microscales for purposes of obtaining $\tilde{T}$ and $\tilde{W}$. Figure 6 shows the effect of the y^+ location, at which the Taylor microscales are evaluated, on the slope of the curve fits, defined as

$$W/\lambda(y^+) \propto (\delta^+)^{A(y^+)}, \tag{7}$$

$$T/\lambda_t(y^+) \propto (\delta^+)^{B(y^+)}. \tag{8}$$

The error bars indicate the uncertainty in the estimation of the slope based on the covariance matrix of the curve fit parameters obtained from the nonlinear regression analysis, which accounts for uncertainties in the magnitudes of δ^+, W, and T; see Ref. [46] for an example of the application of this method. The case of $A = B = 0$ characterizes the proper normalization, i.e., δ^+ independence of $\tilde{T}$ and $\tilde{W}$. One can notice a range of y^+ values between about 50 and 200 wherein the curve fits yield nearly identical slopes regardless of y^+. In this range, both slopes A and B are close to zero to within the uncertainty of the data and analysis. Note that part of the uncertainty stems from the fact that the pocket data and Taylor microscale measurements from the field studies were acquired at different friction Reynolds numbers, with the differences being as much as $\Delta\delta^+ = 5 \times 10^5$ in some cases. The rms of the residual associated with A and B over the range $50 \lesssim y^+ \lesssim 200$ is around 3.5%. The rms of the residuals span between 1.6% and 5.6% over the entire y^+ range shown in Fig. 6. Therefore, the curve fits in (7) and (8) using λ and λ_t values in the range $50 \lesssim y^+ \lesssim 200$, respectively, are deemed good fits to the data.

IV. DISCUSSION AND CONCLUSION

The present study along with [15] establishes that, when inner normalized, the length and time scales of coherent motions detected in the sublayer consist of both a Reynolds-number-invariant component (streaks) and a Reynolds-number-dependent component (pockets). The latter is likely a consequence of spatially compact motions above the sublayer that impart their signature on the sublayer. Apparently these motions play an increasingly important role on near-wall dynamics with increasing Reynolds number [24]. Conceptually, one can think of the pocket size and time interval between pockets as having a connection with some family of eddies that gains proximity to the

wall. Possibilities include, but may not be limited to, typical eddies [7], the heads of hairpinlike vortices that lift out of the sublayer [27], and vortices associated with the more recently identified turbulent-turbulent spots [14]. The present data indicate that if the scale of the (eddy) motion is measured in Taylor units, then the proximity of the eddy to the wall (as measured in viscous units), whereby a pocket formation may be induced, remains nominally invariant with Reynolds number. In fact, the present study suggests that this wall-normal location is $50 \lesssim y^+ \lesssim 200$.

Several interesting coincidences are noted. The location $y^+ = 100$ lies near the lower edge of the "traditional" logarithmic layer (observed in the inner normalized mean streamwise velocity profile) and also corresponds to the location at which a shoulder or plateau begins to emerge in the inner normalized rms streamwise velocity profile. Note that a compilation of streamwise velocity statistics over a very large Reynolds-number range may be found elsewhere [24,39,40]. The inner normalized rms spanwise vorticity profiles also exhibit a noticeable knee (change in slope) in the region $50 \lesssim y^+ \lesssim 120$ that appears to be nearly invariant with Reynolds number [47]. In connection with this, we note that analysis of the mean enstrophy equation reveals that the region interior to $y^+ \simeq 50$ is marked by a rapid decrease in the mean vorticity magnitude [22]. This coincides with a transfer of mean to fluctuating enstrophy and thus physically attributed to the three dimensionalization of the vorticity field into more spatially compact motions. Consistent with this, observations of the premultiplied streamwise velocity spectra reveal that, over a very large Reynolds-number range, the region of interest lies between the inner spectral peak (characteristic of the near-wall cycle) and the midlayer peak associated with the motions that modulate the near-wall flow [20,48]. In relation to coherent motions, we also note that Tomkins and Adrian [49] found that merging vortex packets provide an important mechanism of spanwise growth in the boundary layer up to a distance of about $y^+ = 100$, for the δ^+ range they considered. This is relevant to the present study because "merging structures are expected to leave a highly distinctive footprint or signature in the flow field" and sublayer pockets may reflect this signature. Finally, Stanislas *et al.* [50] observed a difference in vortex characteristics and behavior above $y^+ \approx 100$, compared to the region below that. In particular, their measurements reveal that the characteristic size of eddies increases from the wall and, for $y^+ > 150$, tends to nearly a constant value, which remains independent of Reynolds number when scaled by the local Kolmogorov length.

Interestingly, however, Reynolds-number dependences in the present pocket width data do not scale with the local Kolmogorov length. Figure 7 attests to this fact by showing the Reynolds-number invariance of the inner normalized Kolmogorov length η^+, estimated using the local isotropy assumption, which has been shown to correspond closely to the full dissipation rate outside of the buffer layer [51]. Therefore, in terms of pocket width scaling, W/η behaves like W^+. If sublayer pocket events are indeed believed to be linked to the existence of eddies in the lower logarithmic layer, then the question arises as to why the Kolmogorov length fails to scale the pocket width, when previous works [50,52] indicate that the radius of eddies in the logarithmic region does appear to scale with the Kolmogorov length.

Undoubtedly, many factors affect the response of the sublayer to the motion of eddies above it (i.e., in the form of pocket events). It may be rationally hypothesized, however, that the primary factors driving this interaction are the vortical intensity of the eddy, the size of the eddy, and the propagation velocity (magnitude or direction) of the eddy. The near invariance of the ω_z^+ and ω_y^+ intensities with Reynolds number [47] suggests that the vortical intensity of an initiating eddy at $y^+ \approx 100$ does not vary appreciably with Reynolds number. Therefore, one might surmise that the Reynolds-number dependence of the characteristic pocket scales has less to do with the vortical intensity of the initiating eddy and more to do with its size and/or propagation velocity. However, since eddy size normalized by the Kolmogorov length appears to be independent of Reynolds number at least in the logarithmic region [50,52], one is left deducing that the local propagation velocity provides the major influence in determining characteristic pocket scales.

Given the proposed hypothesis stated above along with the present evidence that the Taylor microscale at $y^+ \approx 100$ exhibits the same Reynolds-number dependence as pocket scales, one may aptly infer that sublayer pockets represent the footprints of wallward-moving coherent

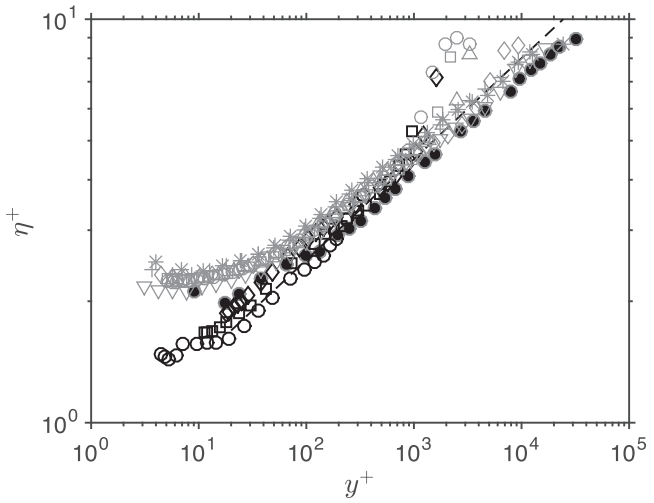

FIG. 7. Inner normalized Kolmogorov length versus inner normalized distance from the wall. Markers are the same as in Fig. 3, except all of the atmospheric data at $\delta^+ = 2.2 \times 10^5$ are plotted as black circles here. The dashed line represents $\eta^+ = (\kappa y^+)^{1/4}$.

vortical structures initially residing at $y^+ \approx 100$ independent of Reynolds number. The important modifier here is the *wallward motion* of the eddy. Further corroboration and qualification of this phenomenological picture is provided by Metzger *et al.* [44], wherein the burst period (or frequency) scaled by the local Taylor microscale was found to be both independent of Reynolds number and wall-normal position. Note that burst events are generally accepted to consist of a sweep of high-momentum fluid toward the wall accompanied by an ejection of low-momentum fluid away from the wall [6]. The equivalency in the scaling properties of (i) the time interval between sublayer pocket events and (ii) the burst period strongly suggests that sublayer pocket events may be attributed to and visually signify the occurrence of a sweep.

A simple scaling argument for pocket width W^+ is presented to examine this idea further. Consider the scenario illustrated in Fig. 8 whereby an eddy of characteristic size ℓ^+ and initially residing in the inner layer at a height of $y^+ \approx 100$ begins to propagate toward the wall at a velocity $\vec{V}_p^+$. When this structure impacts the wall, the footprint is expected to have a length L^+ greater than ℓ^+ due to

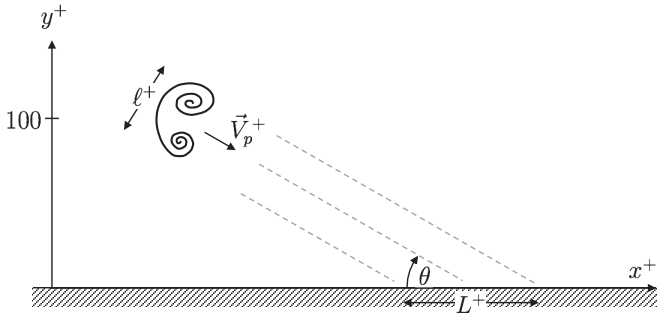

FIG. 8. Schematic of an eddy that initiates from the inner layer (at $y^+ \approx 100$) and propagates toward the wall with a velocity $\vec{V}_p^+$. For a given characteristic size ℓ^+ of the eddy, the footprint at the wall (in the form of a pocket event) is expected to extend a length L^+ due to the acute angle of propagation θ.

the acute angle of propagation θ. From geometry, the length of the footprint is

$$L^+ = \frac{\ell^+}{\sin\theta} \, . \tag{9}$$

Assuming that the eddy propagates in a straight line, the propagation angle θ can be determined from the components of the propagation velocity $\vec{V}_p^+ = u_p^+ \hat{i} + v_p^+ \hat{j}$, where u_p and v_p denote the horizontal and vertical velocity components, respectively. We further assume that the width of the pocket is approximately equal to its length ($W^+ \approx L^+$). Plan-view flow visualization videos reveal pockets to be quasicircular structures, thus substantiating this assumption. This leads to a relation for pocket width of the form

$$W^+ = \frac{\ell^+}{v_p^+} \sqrt{(u_p^+)^2 + (v_p^+)^2} \, . \tag{10}$$

In the analysis below, we show how (10) can be manipulated to obtain a logarithmic Reynolds-number dependence of the inner normalized pocket width consistent with observations from the experimental data in Fig. 4. In order to proceed, we make a number of simplifying assumptions. First of all, it is assumed throughout that the wallward-moving eddy initially resides at $y^+ = 100$. Second, as mentioned earlier, Stanislas *et al.* [50] indicate the mean diameter of vortices in the logarithmic layer normalized by the Kolmogorov scale is $\ell/\eta \approx 20$ independent of Reynolds number. Using the relation $\eta = (\kappa\, y^+)^{1/4}$ yields a characteristic eddy size of $\ell^+ \approx 50$ (based on values of $\kappa = 0.38$ and $y^+ = 100$). Third, it is reasonable to imagine that the propagation velocity components will be similar to the root mean square velocity of the turbulence at the initiating height of the eddy, taken here to be $y^+ = 100$. This gives $u_p^+ \approx (U^+)_{y^+=100} + (u'^+)_{y^+=100}$ and $v_p^+ \approx (v'^+)_{y^+=100}$, where the uppercase and lowercase letters denote the mean and fluctuating (standard deviation) velocities, respectively. It is well known that U^+ is Reynolds number independent in the logarithmic layer [18] with a value of approximately 17 at $y^+ = 100$. Similarly, v'^+ has also been shown to be Reynolds number independent (for moderate to high Reynolds numbers) with a value of 1.16 in the logarithmic layer [47]. Therefore, the only quantity in the relation describing W^+ that exhibits Reynolds-number dependence is u'^+. In fact, Marusic *et al.* [53] suggest a logarithmic dependence of the form $(u'^+)^2 = B_1 - A_1 \log(y^+/\delta^+)$. That study examined a number of experimental data sets yielding a range of values for A_1 and B_1. For purposes of the scaling analysis here, the average values of $A_1 = 1.25$ and $B_1 = 2.2$ are considered. Substituting this relation into (10) and performing some algebraic manipulation, one can show that to leading order

$$W^+ \sim [\log(\delta^+)]^{1/4} \, , \tag{11}$$

where the proportionality constant is equal to $\ell^+ A_1^{1/4} \sqrt{2\,(U^+)_{y^+=100}}/(v'^+)_{y^+=100}$. Plugging in the values stated above for each of the quantities yields a Reynolds-number growth rate of 266 for the inner normalized pocket width, i.e., $W^+ \approx 266[\log(\delta^+)]^{1/4}$ to leading order. This slightly underpredicts (by only a few percent) the behavior of the data, which exhibit a growth rate of 274 when curve fit to the scaling relation in (11). Note that the R^2 value of this curve fit, i.e., $W^+ = a[\log(\delta^+)]^{1/4} + b$, is 0.991, indicating the data fit well to this scaling model. The agreement between the scaling analysis and the data is quite remarkable considering the assumptions and simplicity of the propagation model utilized. Given this, it is not surprising that the Taylor microscale evaluated at $y^+ \approx 100$ succeeds in removing Reynolds-number dependences in the pocket width, since the Taylor microscale inherently incorporates information about the local streamwise turbulent velocity by definition.

In summary, the present results support the physical picture of the near-wall self-sustaining process based on the "parent-offspring autoregeneration mechanism" as described in the recent study of Wu *et al.* [14] and in accord with earlier work [9,27,54–56]. In this picture, viscous sublayer streaks behave as passive entities, frequently perturbed by turbulent-turbulent spots (TUTSs) that are generated locally within the viscous sublayer and buffer layer. Turbulent-turbulent spots appear to

originate from hairpin vortex packets occupying the near-wall region and as such are characterized by spatially intermittent concentration of small-scale vortices. Wu *et al.* revealed that TUTSs are structurally analogous to transitional-turbulent spots that form as part of the secondary instability in laminar boundary layer transitions. In their DNS visualizations, they noticed that indented sublayer streaks often simply form the edges of pockets that arise from the existence of TUTSs. The present results appear consistent with this connection between pockets and TUTSs. Specifically, we have shown that (i) pockets scale with the Taylor microscale measured at $y^+ \approx 100$, which is in the same wall-normal region where TUTSs largely reside, and (ii) the Reynolds-number growth of the inner normalized pocket width W^+ can be obtained from a simple model of a compact vortex located at $y^+ \approx 100$ that propagates obliquely toward the wall. It remains to be seen whether the disturbances leading to pocket formation in the sublayer are responsible for instigating the birth of infant TUTSs or whether pockets are mere footprints of compact vortical motions from more mature TUTSs aloft. In either case, future work is needed to determine if there are specific events that initiate the wallward motion of pocket-producing eddies and how this overall picture of the near-wall process is linked to the observation of a hierarchy of large-scale and very-large-scale motions [48,57] farther from the wall. In this regard, determining the relative contributions of TUTSs to wall-layer turbulence production (versus the self-sustaining process associated with streaks and quasistreamwise vortices [10]) would seem to be an important factor.

ACKNOWLEDGMENTS

Support by the Office of Naval Research (Grant No. N00014-04-1-0304) and National Science Foundation (Grants No. CTS-0120061 and No. CBET-0555223) is gratefully acknowledged.

[1] T. Theodorsen, *Proceedings of the Second Midwestern Conference on Fluid Mechanics* (Ohio State University, Columbus, 1952), Vol. 149, pp. 1–19.
[2] S. J. Kline, W. C. Reynolds, F. A. Schraub, and P. W. Runstadler, The structure of turbulent boundary layers, J. Fluid Mech. **30**, 741 (1967).
[3] E. Corino and R. Brodkey, A visual investigation of the wall region in turbulent flow, J. Fluid Mech. **37**, 1 (1969).
[4] G. Offen and S. Kline, A proposed model of the bursting process in turbulent boundary layers, J. Fluid Mech. **70**, 209 (1975).
[5] B. Cantwell, Organized motion in turbulent flow, Annu. Rev. Fluid Mech. **13**, 457 (1981).
[6] S. K. Robinson, Coherent motions in the turbulent boundary layer, Annu. Rev. Fluid Mech. **23**, 601 (1991).
[7] R. Falco, A coherent structure model of the turbulent boundary layer and its ability to predict Reynolds number dependence, Philos. Trans. R. Soc. London A **336**, 103 (1991).
[8] M. Gad-el-Hak and P. Bandyopadhyay, Reynolds number effects in wall-bounded turbulent flows, Appl. Mech. Rev. **47**, 307 (1994).
[9] R. Adrian, Hairpin vortex organization in wall turbulence, Phys. Fluids **19**, 041301 (2007).
[10] F. Waleffe, On a self-sustaining process in shear flows, Phys. Fluids **9**, 883 (1997).
[11] J. Jiménez and A. Pinelli, The autonomous cycle of near-wall turbulence, J. Fluid Mech. **389**, 335 (1999).
[12] W. Schoppa and F. Hussain, Coherent structure generation in near-wall turbulence, J. Fluid Mech. **453**, 57 (2002).
[13] E. Falco, New Results, A Review and Synthesis of the Mechanism of Turbulence Production in Boundary Layers and its Modification, AIAA 21st Aerospace Sciences Meeting, Reno, NV, January 10-13, Paper AIAA-83-0377 (1983).
[14] X. Wu, P. Moin, J. Wallace, J. Skarda, A. Lozano-Duran, and J.-P. Hickey, Transitional-turbulent spots and turbulent-turbulent spots in boundary layers, Proc. Natl. Acad. Sci. USA **114**, E5292 (2017).
[15] J. C. Klewicki, M. M. Metzger, E. Kelner, and E. M. Thurlow, Viscous sublayer flow visualizations at $R_\theta \approx 1500000$, Phys. Fluids **7**, 857 (1995).

[16] C. R. Smith and S. P. Metzler, The characteristics of low-speed streaks in the near-wall region of a turbulent boundary layer, J. Fluid Mech. **129**, 27 (1983).
[17] J. Klewicki, Reynolds number dependence, scaling and dynamics of turbulent boundary layers, J. Fluids Eng. **132**, 094001 (2010).
[18] I. Marusic, B. J. McKeon, P. A. Monkewitz, H. M. Nagib, A. J. Smits, and K. R. Sreenivasan, Wall-bounded turbulent flows: Recent advances and key issues, Phys. Fluids **22**, 065103 (2010).
[19] A. J. Smits, B. J. McKeon, and I. Marusic, High Reynolds number wall turbulence, Annu. Rev. Fluid Mech. **43**, 353 (2011).
[20] R. Mathis, N. Hutchins, and I. Marusic, Large-scale amplitude modulation of the small-scale structures in turbulent boundary layers, J. Fluid Mech. **628**, 311 (2009).
[21] T. Wei, P. Fife, J. Klewicki, and P. McMurtry, Properties of the mean momentum balance in boundary layer, pipe, and channel flows, J. Fluid Mech. **522**, 303 (2005).
[22] J. Klewicki, Self-similar mean dynamics in turbulent wall flows, J. Fluid Mech. **718**, 596 (2013).
[23] C. Chin, J. Philip, J. Klewicki, A. Ooi, and I. Marusic, Reynolds-number-dependent turbulent inertia and onset of log region in pipe flows, J. Fluid Mech. **757**, 747 (2014).
[24] M. M. Metzger and J. C. Klewicki, A comparative study of near-wall turbulence in high and low Reynolds number boundary layers, Phys. Fluids **13**, 692 (2001).
[25] J. Klewicki, P. Priyadarshana, and M. Metzger, Statistical structure of the fluctuating wall pressure and its in-plane gradients at high Reynolds number, J. Fluid Mech. **609**, 195 (2008).
[26] R. Falco, in *Turbulence in Liquids*, edited by G. K. Patterson and J. L. Zakin (University of Missouri–Rolla, Rolla, 1980), pp. 1–14.
[27] C. Smith, J. Walker, A. Haidari, and U. Sobrun, On the dynamics of near-wall turbulence, Philos. Trans. R. Soc. London A **336**, 131 (1991).
[28] S. Robinson, S. Kline, and P. Spalart, A review of quasi-coherent structures in a numerically simulated turbulent boundary layer, NASA Report No. NASA/TM-102191, 1989.
[29] R. Falco, J. Klewicki, and K. Pan, in *Structure of Turbulence and Drag Reduction*, edited by A. Gyr (Springer, Berlin, 1990), pp. 59–68.
[30] R. Falco, Coherent motions in the outer region of turbulent boundary layers, Phys. Fluids **20**, S124 (1977).
[31] M. J. Lighthill, in *Laminar Boundary Layers*, edited by L. Rosenhead (Oxford University Press, New York, 1963), pp. 48–88.
[32] J. Klewicki and R. Falco, Spanwise vorticity structure in turbulent boundary layers, Int. J. Heat Fluid Flow **17**, 363 (1996).
[33] J. Jiménez, P. Moin, R. Moser, and L. Keefe, Ejection mechanisms in the sublayer of a turbulent channel, Phys. Fluids **31**, 1311 (1988).
[34] J. Klewicki, C. Gendrich, J. Foss, and R. Falco, On the sign of the instantaneous spanwise vorticity component in the near-wall region of turbulent boundary layers, Phys. Fluids A **2**, 1497 (1990).
[35] S. Rajagopalan and R. Antonia, Structure of the velocity field associated with the spanwise vorticity in the wall region of a turbulent boundary layer, Phys. Fluids A **5**, 2502 (1993).
[36] J. Klewicki, A description of turbulent wall-flow vorticity consistent with mean dynamics, J. Fluid Mech. **737**, 176 (2013).
[37] Y. Wu and K. Christensen, Population trends of spanwise vortices in wall turbulence, J. Fluid Mech. **568**, 55 (2006).
[38] A. Fershtut, On the Reynolds number dependence of passive contaminant motions in the viscous sublayer, M.S. thesis, University of Utah, 2006.
[39] M. Metzger, B. McKeon, and H. Holmes, The near-neutral atmospheric surface layer: Turbulence and non-stationarity, Philos. Trans. R. Soc. A **365**, 859 (2007).
[40] M. Metzger, Length and time scales of the near-surface axial velocity in a high Reynolds number turbulent boundary layer, Int. J. Heat Fluid Flow **27**, 534 (2006).
[41] P. Vincenti, J. Klewicki, C. Morrill-Winter, C. M. White, and M. Wosnik, Streamwise velocity statistics in turbulent boundary layers that spatially develop to high Reynolds number, Exp. Fluids **54**, 1629 (2013).
[42] J. Klewicki, On the interactions between the inner and outer region motions in turbulent boundary layers, Ph.D. thesis, Michigan State University, 1989.

[43] H. Tennekes and J. L. Lumley, *A First Course in Turbulence* (MIT Press, Cambridge, 1972).
[44] M. Metzger, B. J. McKeon, and E. Arce-Larreta, Scaling the characteristic time of the bursting process in the turbulent boundary layer, Physica D **239**, 1296 (2010).
[45] P. Priyadarshana and J. Klewicki, in *Reynolds Number Scaling in Turbulent Flows*, edited by J. A. Smits (Kluwer Academic, Dordrecht, 2003), pp. 117–123.
[46] M. Metzger, Scalar dispersion in high Reynolds number turbulent boundary layers, Ph.D. thesis, University of Utah, 2002.
[47] P. Priyadarshana, J. Klewicki, S. Treat, and J. Foss, Statistical structure of turbulent-boundary-layer velocity-vorticity products at high and low Reynolds numbers, J. Fluid Mech. **570**, 307 (2007).
[48] N. Hutchins and I. Marusic, Evidence of very long meandering features in the logarithmic region of turbulent boundary layers, J. Fluid Mech. **579**, 1 (2007).
[49] C. Tomkins and R. Adrian, Spanwise structure and scale growth in turbulent boundary layers, J. Fluid Mech. **490**, 37 (2003).
[50] M. Stanislas, L. Perret, and J.-M. Foucaut, Vortical structures in the turbulent boundary layer: A possible route to a universal representation, J. Fluid Mech. **602**, 327 (2008).
[51] J. C. Klewicki and R. E. Falco, On accurately measuring statistics associated with small-scales in turbulent boundary layers using hot-wire probes, J. Fluid Mech. **219**, 119 (1990).
[52] M. Tanahashi, S.-J. Kang, T. Miyamoto, S. Shiokawa, and T. Miyauchi, Scaling law of fine scale eddies in turbulent channel flows up to $\mathrm{Re}_\tau = 800$, Int. J. Heat Fluid Flow **25**, 331 (2004).
[53] I. Marusic, J. P. Monty, M. Hultmark, and A. J. Smits, On the logarithmic region in wall turbulence, J. Fluid Mech. **716**, 1 (2013).
[54] J. Zhou, R. J. Adrian, S. Balachandar, and T. M. Kendall, Mechanisms for generating coherent packets of hairpin vortices in channel flow, J. Fluid Mech. **387**, 353 (1999).
[55] R. Panton, Overview of the self-sustaining mechanisms of wall turbulence, Prog. Aerosp. Sci. **37**, 341 (2001).
[56] R. Adrian, C. Meinhart, and C. Tomkins, Vortex organization in the outer layer region of the boundary layer, J. Fluid Mech. **422**, 1 (2000).
[57] Y. H. Lee and H. J. Sung, Very-large-scale motions in a turbulent boundary layer, J. Fluid Mech. **673**, 80 (2011).